nature communications

Article

https://doi.org/10.1038/s41467-026-71399-8

3D-printed NiTi alloys for elastocaloric cooling

Received: 19 November 2025

Accepted: 18 March 2026

Shiyu Zhong[1,2,5], Hongyang Lin[3,5], Yang Li[3], Ying Li[2,4], Guoan Zhou[3], Peiyuan Zhang[3], Lei Zhang[1], Shuo Wang[1], Shuhuai Yao[3] ✉, Qingping Sun[3] ✉ & Jian Lu[1,2,4] ✉

NiTi-based elastocaloric cooling presents an environmentally friendly solid-state alternative to vapor-compression refrigeration. However, conventional NiTi refrigerant fabrication relies on thermomechanically intensive processes that limit geometric versatility while increasing production time, costs, and material waste. Although 3D printing offers a potential solution, existing 3D-printed NiTi alloys face a critical trade-off between cyclic durability and specific temperature change (the adiabatic temperature change per unit driving stress). Here, we address these challenges by developing a high-performance 3D-printed NiTi alloy with defect-minimized, bimodal microstructures. This design facilitates stress-induced martensitic phase transformation while suppressing dislocation slip and crack propagation. Consequently, the alloys can withstand a record-high 3 million cycles without failure, while simultaneously achieving an 11-fold enhancement in specific temperature change over state-of-the-art 3D-printed counterparts (increasing from 2.97 to 33.6 °C·GPa^{-1}). Furthermore, we realize direct 3D printing and integration of NiTi refrigerants into a macroscale cooling prototype, which achieves a temperature span of 20 °C. Our work establishes 3D-printed NiTi alloys as viable elastocaloric refrigerants, unlocking a 3D-printing-enabled pathway toward sustainable cooling systems.

Space cooling is becoming increasingly essential due to global warming. It is achieved primarily through vapor-compression refrigeration – a technology reliant on fluorinated greenhouse gases, which exacerbate climate change[1]. This critical sustainability gap is driving demand for alternatives. Solid-state elastocaloric cooling using NiTi alloys has emerged as a promising solution, offering zero direct emissions and high energy density[2–4]. When strained at temperatures above their austenite finish temperature (A_f), NiTi alloys undergo stress-induced phase transformation, delivering adiabatic temperature changes (ΔT) larger than 10 °C[5]. Elastocaloric cooling prototypes featuring NiTi-based refrigerants that leverage this effect have been demonstrated worldwide[6–18].

However, fabricating high-performance NiTi refrigerants typically requires intensive thermomechanical processing, such as multi-pass rolling, multiple heat treatments, and electrical discharge machining (EDM)[12,13,19–22]. These energy-intensive processes substantially increase manufacturing costs and material waste. Moreover, they rigidly constrain the geometries of NiTi refrigerant flow channels, fundamentally limiting design flexibility and performance ceilings. An attractive approach to addressing these challenges is three-dimensional (3D)

---

[1]Department of Mechanical Engineering, City University of Hong Kong, Hong Kong, China. [2]Research Department on Advanced Structural Materials and Additive Manufacturing, City University of Hong Kong Matter Science Research Institute (Futian), Shenzhen, China. [3]Department of Mechanical and Aerospace Engineering, The Hong Kong University of Science and Technology, Hong Kong, China. [4]Centre for Advanced Structural Materials, City University of Hong Kong Shenzhen Research Institute, Shenzhen, China. [5]These authors contributed equally: Shiyu Zhong, Hongyang Lin. ✉e-mail: meshyao@ust.hk; meqpsun@ust.hk; jianlu@cityu.edu.hk

printing. By enabling selective, rapid melting and solidification of materials based on digital models, the on-demand additive manufacturing paradigm significantly reduces material waste while overcoming geometric constraints inherent to conventional processing techniques[23–26].

Accordingly, the following question arises: Can 3D-printed NiTi alloys perform comparably to conventionally manufactured NiTi counterparts? Most 3D-printed NiTi alloys reported to date exhibit lifespans below 1000 cycles – orders of magnitude lower than the million-cycle durability required for practical applications[27–37]. Only one pioneering design, incorporating a 50 vol.% Ni_3Ti reinforcing phase into a 3D-printed NiTi composite, achieves million-cycle durability[38]. Nevertheless, this high-modulus non-transforming phase induces a high driving stress (σ_{DRI}) of ~1400 MPa, while the resulting ΔT remains below 4 °C. Consequently, this fatigue-resistant 3D-printed NiTi alloy exhibits an unsatisfactory specific temperature change (ΔT_{spe}, adiabatic temperature change per unit driving stress) of less than 3 °C·GPa^{-1}. This performance contrasts with that of commercial NiTi alloys, which show million-cycle durability and ΔT_{spe} levels reaching 15–20 °C·GPa^{-1} [19,39,40]. Thus, resolving the cycling durability–ΔT_{spe} trade-off is pivotal to unleashing 3D printing's significant potential for sustainable cooling.

Herein, we report 3D-printed NiTi alloys with million-cycle durability and a ΔT_{spe} of over 30 °C·GPa^{-1}. This performance breakthrough is attributed to the regulation of metallurgical defects and the development of bimodal microstructures. Moreover, we demonstrate a functional cooling device employing 3D-printed NiTi refrigerants, representing a critical step towards practical solid-state cooling.

Elastocaloric cooling performance of 3D-printed NiTi alloys

The elastocaloric performance of NiTi alloys is governed by stress-induced martensitic transformation, which necessitates precise stress regulation to balance competing mechanisms. To optimize ΔT_{spe}, we established quantitative stress–transformation–cooling correlations through uniaxial compression experiments (Fig. S1 and Supplementary Note 1). Separate samples were used for each stress level to isolate the effect of σ_{DRI} from any prior loading history. In brief, the stress–strain curve exhibits sequential elastic, transformation, and plastic deformation regimes. The corresponding ΔT begins at 2.4 °C under 300 MPa, peaks at 19.5 °C under 550 MPa, and declines to 4.5 °C under 1000 MPa. This trend arises from insufficient phase transformation under low stress and irreversible plasticity under excessive stress, both of which lead to a low ΔT. Therefore, 550 MPa is identified as the optimal σ_{DRI}, which balances adequate phase transformation with minimal plastic deformation. This amount of stress is expected to maximize ΔT_{spe} while minimizing cyclic damage, thereby extending cyclic durability.

We then conducted cyclic compression tests under 550 MPa for 3 × 10^6 cycles to evaluate the cycling durability and long-term elastocaloric performance of the NiTi alloys (Fig. 1a, b). The initial cycle ($N = 1$) exhibits a ΔT approaching 20 °C, accompanied by a 13.4 MJ·m^{-3} hysteresis and 1.1% residual strain (Fig. S2). The residual strain is attributed primarily to transformation-induced dislocations and dislocation-pinned residual martensite[41], as indicated in Fig. S3. By $N = 100$ cycles, a near-self-stabilization stage is achieved, which reduces the hysteresis to 1–2 MJ·m^{-3} and the residual strain to <0.3% (Fig. S2). However, the reversible phase transformation is compromised by residual martensite accumulation, which results in a ΔT of 11.4–13.4 °C (Fig. 1b). This functional degradation is a common issue and is observed in commercial NiTi alloys as well[39] (Fig. S4). Significantly, our 3D-printed NiTi alloys withstand three million cycles without fracture, as confirmed by the results of three independent tests conducted to demonstrate repeatability.

Figure 1c plots the maximum ΔT_{spe} versus the highest reported cycle count of various 3D-printed NiTi alloys and conventional counterparts. For a fair comparison, the maximum ΔT_{spe} values are based on the first-cycle ΔT presented for each alloy, unless otherwise specified in the literature. More details are provided in Methods and Supplementary Table 1. A significant trade-off exists with 3D-printed NiTi alloys: while some variants demonstrate high ΔT_{spe} values of 15–20 °C·GPa^{-1}, their reported cycles are limited to fewer than 100; the state-of-the-art 3D-printed NiTi alloy achieves a remarkable endurance of up to a million cycles but displays a low ΔT_{spe} of less than 3 °C·GPa^{-1} [38]. In contrast, our 3D-printed NiTi alloys exhibit a durability of three million cycles, which is the highest reported value among 3D-printed NiTi alloys for elastocaloric cooling applications. Moreover, our alloys demonstrate a maximum ΔT_{spe} of 33.6 °C·GPa^{-1}, achieving an 11-fold enhancement over the abovementioned benchmark[38]. Even after three million cycles, our alloys retain a high ΔT_{spe} of 20.7 °C·GPa^{-1}, which rivals the maximum ΔT_{spe} reported for other 3D-printed NiTi alloys. These performance parameters are comparable to, or even surpass, those of commercial NiTi alloys. The findings provide compelling evidence that the cycling durability and ΔT_{spe} of 3D-printed NiTi alloys can be reconciled, confirming the potential of 3D printing for manufacturing high-performance NiTi refrigerants. The following section describes the microstructural design that enables the outstanding performance observed.

Microstructural design of 3D-printed NiTi alloys

The poor fatigue properties of 3D-printed metals result from metallurgical-manufacturing-induced defects and crack-propagation-susceptible microstructures[42–44]. Printing defects (e.g., lack-of-fusion flaws) and insufficient crack-inhibiting microstructures (e.g., coarse columnar grains) impair cycling durability in NiTi alloys. Concurrently, the inadequate dislocation resistance from such microstructures increases the residual martensite content, reducing the proportion of transformable phases and diminishing ΔT. To enhance cycling durability and ΔT_{spe} simultaneously, we engineered defect-refined, bimodal microstructures through laser powder bed fusion (LPBF) following single-step annealing.

The LPBF processing determines the defect contents of 3D-printed alloys. Metallurgical defects typically originate from improper heat input[45]. When the volumetric energy density (*VED*) is excessively high, the melt pool becomes too deep and prone to instability, which results in the formation of keyholes and increases the overall porosity. Conversely, if the *VED* is too low, the energy is insufficient to fully melt the powder, which leads to a lack of fusion. By employing an optimized *VED* of 56.3 J·m^{-3}, we avoid both types of defects in our alloys, thereby achieving an ultralow defect density of 0.02% (Fig. S5). Moreover, the fragile coarse columnar grains were eliminated through the optimized printing process, as detailed in Supplementary Note 2.

Subsequently, we implemented annealing to 1) establish bimodal microstructures for crack and dislocation control, and 2) maintain a near-room-temperature A_f for efficient phase transformation. In as-printed NiTi alloys, high-density low-angle grain boundaries (LAGBs, Fig. S6) form through the self-organization of dislocations (Fig. S7), a process driven by the thermal stress arising from the rapid solidification during LPBF. These dislocations should be reduced because they increase transformation temperatures by promoting martensite nucleation[46]. Without increasing the defect content (Fig. 2a), annealing facilitates the annihilation and rearrangement of dislocations, which results in a low dislocation density (Fig. S8) comparable to that of commercial NiTi alloys (Fig. S9). It also converts LAGBs into high-angle grain boundaries (HAGBs), yielding bimodal microstructures comprising 77.7% micron grains and 22.3% refined grain clusters (Fig. 2b). Moreover, sub-micron particles (~2%, area fraction) precipitate after annealing (Fig. 2c) and were confirmed to be the Ti_2Ni phase using energy-dispersive X-ray spectroscopy (EDS), selected area electron diffraction (SAED), and high-resolution transmission electron microscopy (TEM) (Fig. 2d). The Ti-rich phase is believed to lower A_f[47], which

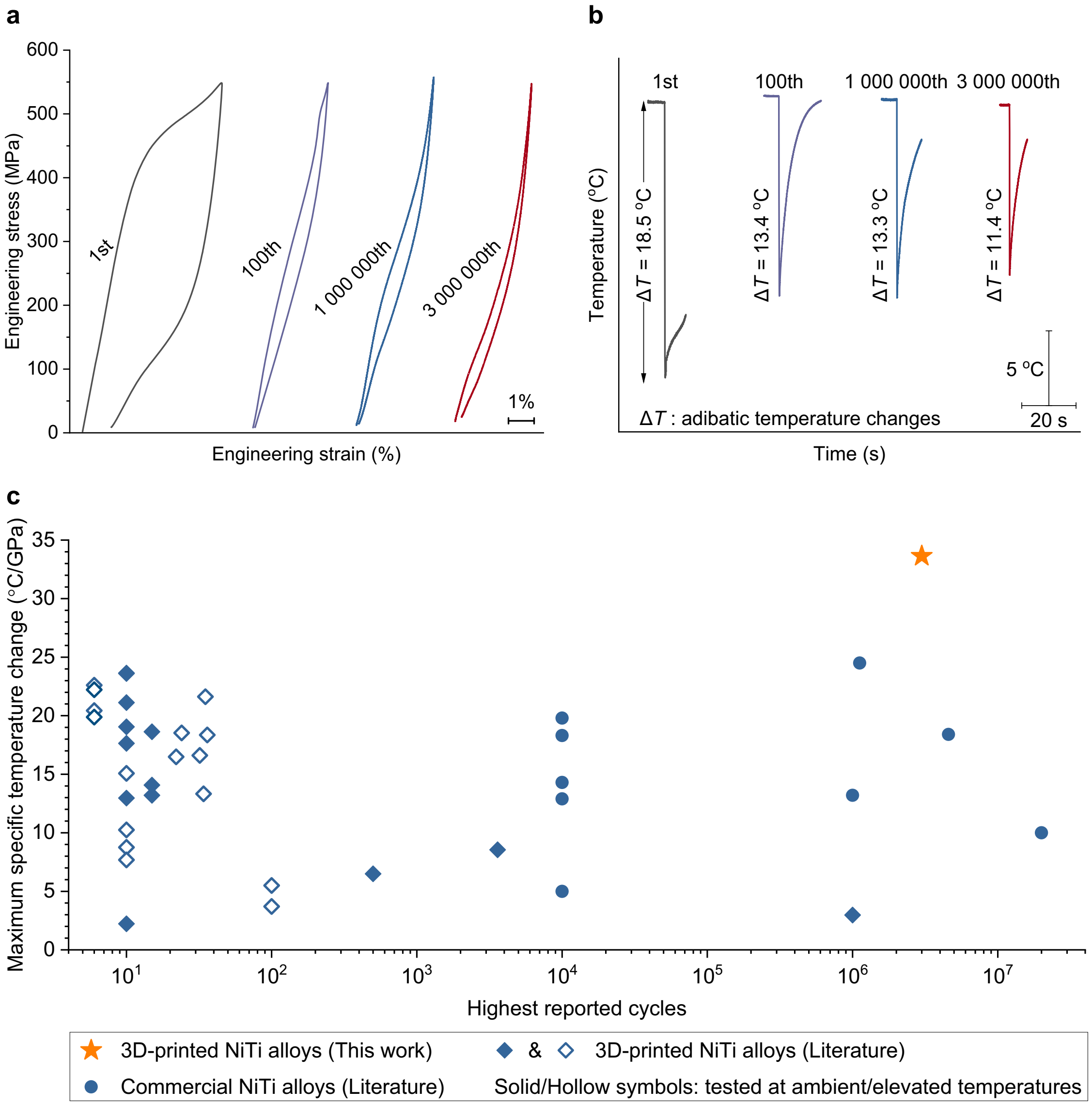

Fig. 1 | Elastocaloric cooling performance of 3D-printed NiTi alloys. **a** Stress–strain curves and **b** corresponding adiabatic temperature changes (ΔT) at different compression cycles. **c** Comparison between alloys in terms of maximum specific temperature change (ΔT_{spe}, defined as the ΔT per unit driving stress) versus the highest reported cycle counts. Our alloys circumvent the trade-off between cycling durability and ΔT_{spe}, surpassing commercial[22,39,49] and other 3D-printed NiTi alloys[27–29,33–38]. ΔT_{spe} is calculated from the first-cycle ΔT reported for each alloy (or as specified in the literature). See Methods and Supplementary Table 1 for more details.

benefits elastocaloric performance as discussed in subsequent sections. Consequently, A_f decreases from 18.5 °C (Fig. S11) to 8.5 °C (Fig. 2e) after annealing, providing the room-temperature-stable austenite phase essential for stress-induced transformation. Figure 2f presents a schematic of bimodal microstructures, distinguishing them from both the coarse columnar grains in other 3D-printed NiTi alloys[48] and the uniform equiaxed grains in commercial NiTi alloys (Fig. S12).

Explanation for enhanced elastocaloric cooling performance of proposed 3D-printed NiTi alloys

Benefiting from the meticulously designed microstructures, our alloys simultaneously achieve high cycling durability and large ΔT_{spe}. The mechanisms underlying these attributes are discussed in the following subsections, along with descriptions of microstructure evolution during cycling.

High cycling durability. Micro-computed tomography (μ-CT) tracking reveals delayed crack nucleation and suppressed growth kinetics in our 3D-printed NiTi alloys. Sparse transverse cracks, initiated by stress concentrations near surface imperfections[49], nucleate after 1 × 10^5 cycles (Fig. 3a). The porosity remains stable at 0.02% during early cycling, rising merely to 0.03% after 1 million cycles. This minimal damage evolution underscores the microstructural fatigue resistance of our alloys.

Crack nucleation resistance arises from a near-defect-free metallurgical condition that eliminates preferential initiation sites. Additionally, high-strength refined grain clusters, which exhibit robust interfacial bonding, act as hard domains that bear primary stress[50], suppressing crack nucleation by accommodating plastic strain gradients via geometrically necessary dislocations at their interfaces[51] (Fig. S13).

Bimodal microstructures further inhibit crack propagation by enhancing crack-path tortuosity to block intergranular fracture paths. Trans-granular cracks perpendicular to the building direction, which emerge after 3 × 10^6 cycles (Fig. 3b), are generally impeded at grain boundaries without unstable intergranular extension. Upon

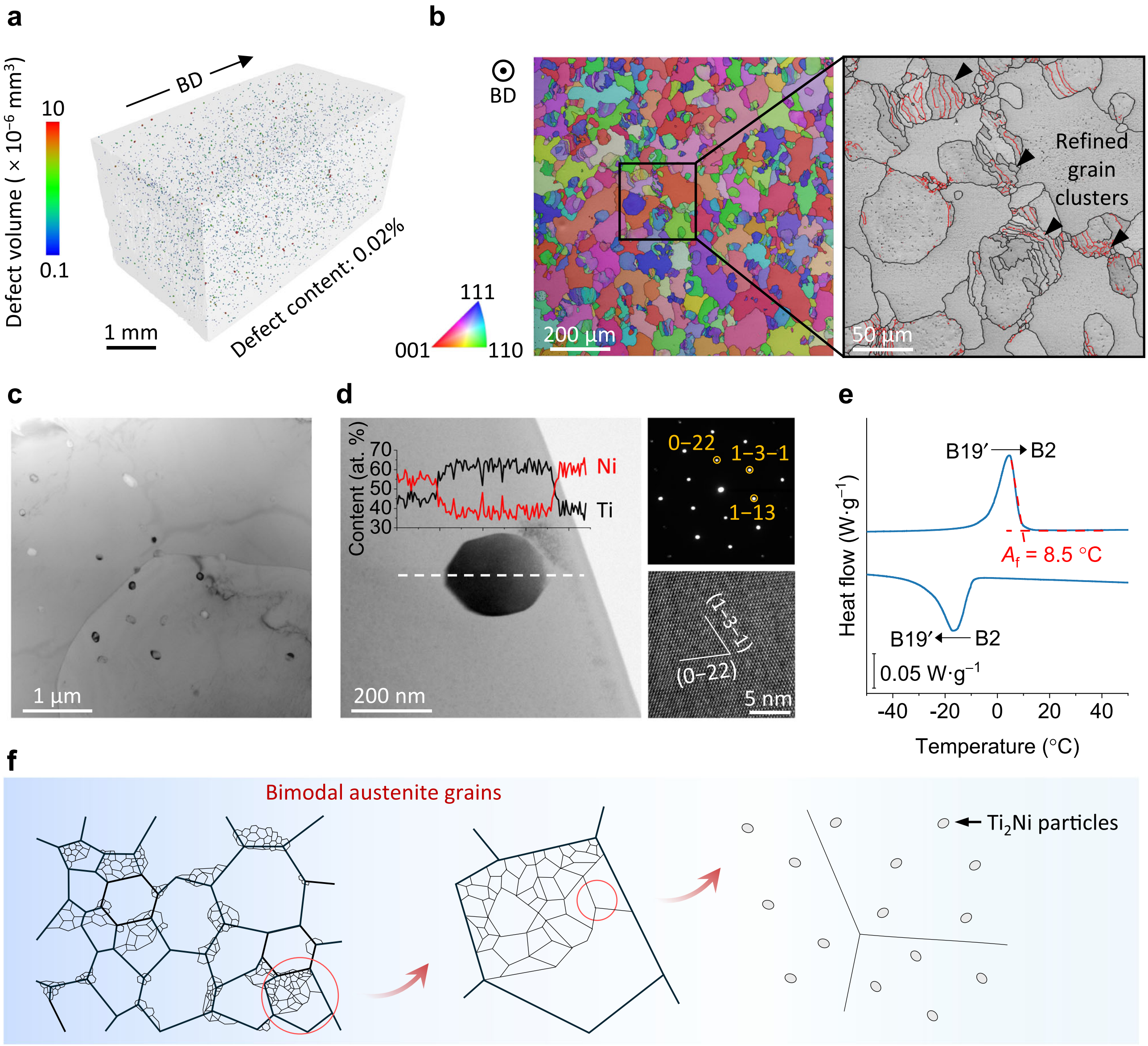

Fig. 2 | Microstructures of 3D-printed NiTi alloys. a Micro-computed tomography (μ-CT) image showing an ultralow defect density (<0.02%; BD: building direction). **b** Electron backscatter diffraction (EBSD) images revealing bimodal grain morphology with micron grains and refined grain clusters. Red lines represent low-angle grain boundaries (2–10°); black lines represent high-angle grain boundaries (>10°). Morphologies along BD are presented in Fig. S10. **c** Transmission electron microscopy (TEM) image depicting dispersed sub-micron particles. **d** High-magnification TEM image of a particle belonging to the Ti$_2$Ni phase, as confirmed by energy-dispersive X-ray spectroscopy (EDS), selected area electron diffraction (SAED), and high-resolution TEM. **e** Differential scanning calorimetry curve illustrating B2–B19′ transformation with an A_f of 8.5 °C. **f** Schematic of bimodal microstructures.

approaching boundaries, the cracks encounter resistance from refined grain clusters, which results in crack deflection, secondary cracking, or crack arrest (Fig. 3b).

Moreover, phase transformation toughening synergizes with bimodal microstructures to enhance crack shielding. Stress concentration at crack tips triggers martensitic transformation in micron grains (Fig. S14), which consumes crack-propagation energy[52] while generating lattice-expansion-induced compressive stress[53]. These dual effects facilitate crack arrest, characterized by the dimensionless parameter $\alpha = \sigma_{tr}\cdot\varepsilon_{tr}/(\sigma_{tr}^2\cdot E^{-1})$, where σ_{tr}, ε_{tr}, and E denote the transformation stress, transformation strain, and austenite elastic modulus, respectively[54]. Compared with refined grains, micron grains exhibit lower σ_{tr} and higher ε_{tr} values, yielding greater values of α and enhancing toughening efficacy[55]. In crack-wake regions, the reverse transformation occurs due to stress relaxation, leading to additional energy dissipation and promoting crack shielding. Thus, the synergistic interplay between martensitic-transformation-induced crack-tip blunting in micron grains and interface-mediated crack blocking by refined grain clusters ensures superior fatigue resistance.

High specific temperature change. Achieving high ΔT_{spe} requires substantial reversible transformation under minimal σ_{DRI}, which necessitates concurrent optimization of thermodynamic stability and microstructural features.

Thermodynamically, maintaining A_f at 5–20 °C below the service temperature stabilizes the transformable phase[21,27,56]. An excessively high A_f induces austenite destabilization and even spontaneous martensite formation under ambient conditions, depleting reversible phase content and suppressing ΔT (Figs. S15–S17). Conversely, an exceedingly low A_f elevates σ_{DRI} based on the Clausius–Clapeyron

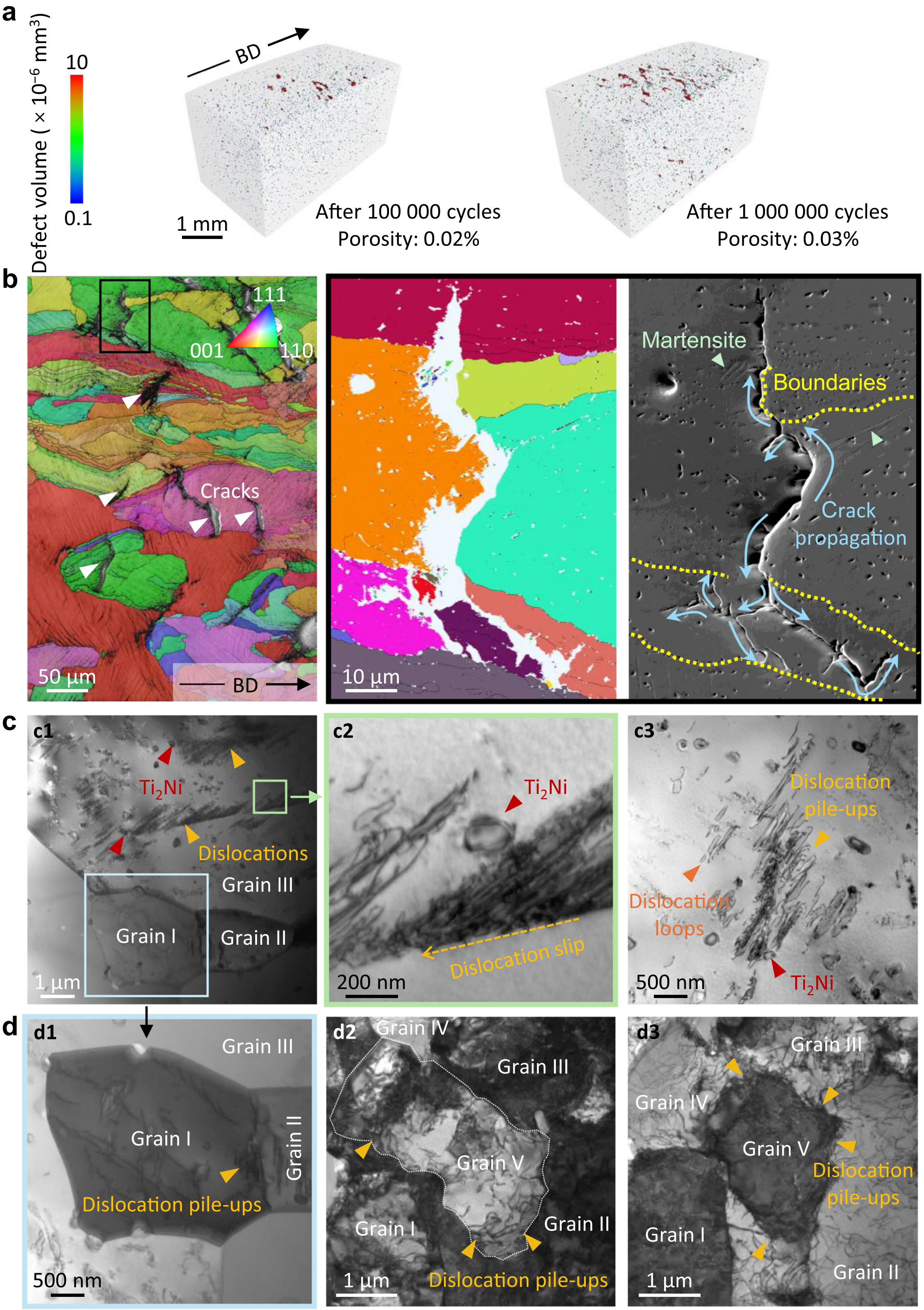

Fig. 3 | Microstructure evolution during cycling. a µ-CT result of the same sample after 1×10^5 and 1×10^6 cycles. **b** EBSD and scanning electron microscopy (SEM) images showing crack morphologies. TEM images illustrating interactions between **c** Ti_2Ni precipitates and dislocations, and **d** grain boundaries and dislocations.

relationship[57] (Figs. S18–S19). Here, we regulate A_f to be approximately 13 °C below the ambient temperature, which preserves austenite dominance while ensuring a low σ_{DRI} (550 MPa).

Microstructurally, plastic deformation and martensitic transformation are competitive mechanisms. Sustaining a high ΔT_{spe} requires suppressing irreversible plastic deformation while facilitating the reversible phase transformation. Inadequate dislocation slip resistance prioritizes irreversible deformation over reversible transformations, whereas dislocation-pinned martensite obstructs reverse transformation, both of which degrade ΔT. 3D-printed NiTi alloys typically exhibit

https://doi.org/10.1038/s41467-026-71399-8

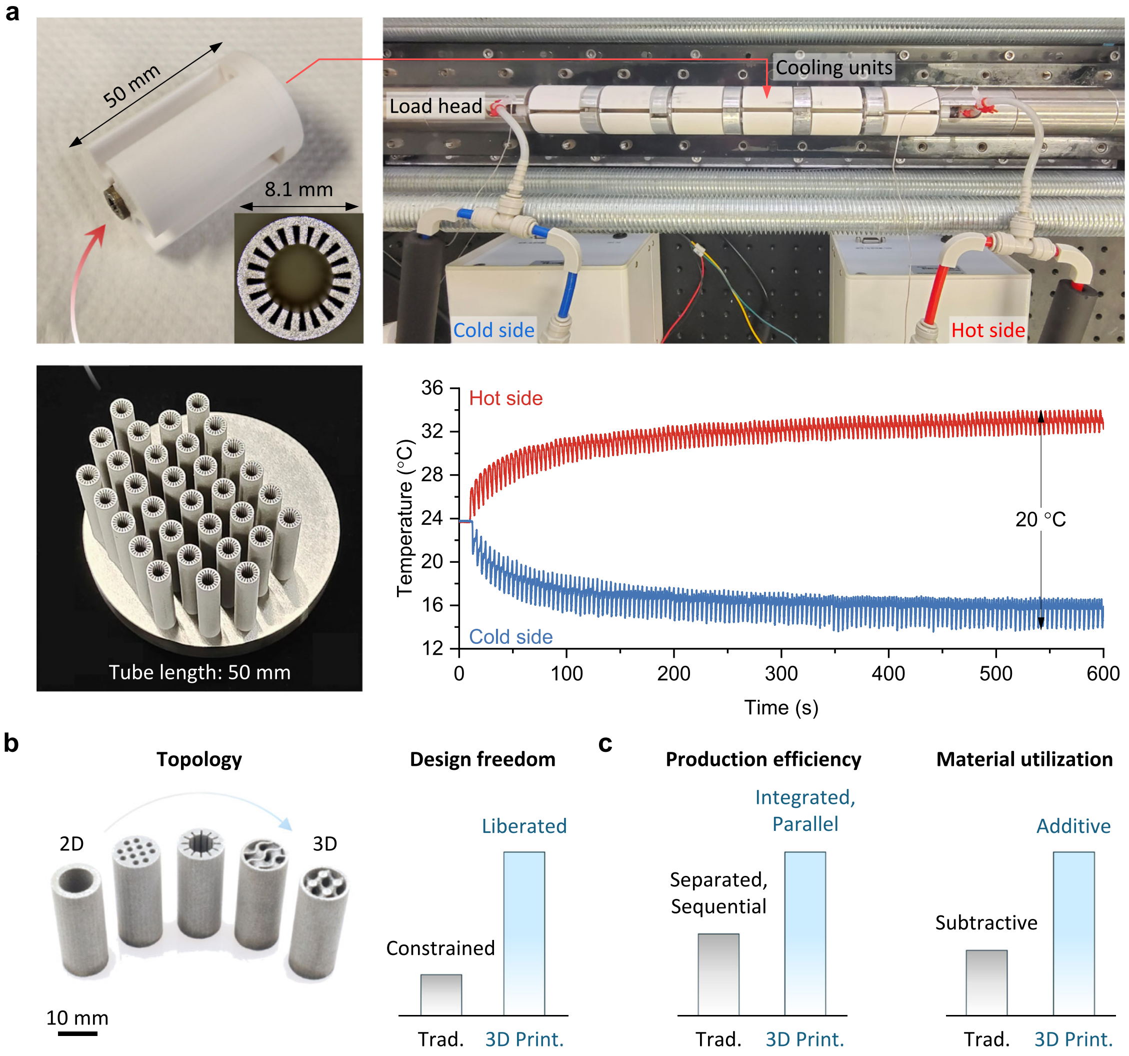

Fig. 4 | 3D-printed NiTi tubes used as refrigerants. a Elastocaloric cooling performance of a prototype utilizing five units of 3D-printed NiTi tubes. **b** 3D-printed NiTi refrigerants in various configurations, highlighting the transformation in fabrication capability from planar (2D) to spatial (3D) channel geometries. 3D Print.: 3D printing; Trad.: traditional processes. **c** Production efficiency and material utilization benefits of 3D printing over traditional processes.

coarse columnar grains[34,48,58], which offer limited resistance to dislocation slip and lead to unsatisfactory properties. These issues are effectively resolved by the bimodal microstructures introduced in this study. As evidenced by ubiquitous pile-ups at interfaces (Fig. 3d), refined grain clusters enhance grain boundary strengthening by shortening the dislocation mean free paths. This significantly improves the overall slip resistance and suppresses plastic deformation. While local Ti_2Ni–dislocation interactions are observed (Fig. 3c), their contribution to strengthening is considered limited, given the low number density and relatively large size of Ti_2Ni[59]. Therefore, the primary strengthening comes from bimodal grain architecture. Moreover, the bimodal microstructures play a pivotal role in promoting martensitic transformation. Specifically, refined grains enhance martensite nucleation, while micron grains facilitate its propagation kinetics[24,60]. With the dual capacity to resist slip and facilitate transformation, the bimodal microstructures ensure ΔT_{spe} retention (>20 °C·GPa^{-1}) over 3 million cycles.

Cooling prototype with 3D-printed NiTi refrigerants

Capitalizing on our breakthroughs in alloy performance, we present a macro-scale elastocaloric refrigeration prototype utilizing 3D-printed NiTi refrigerants. The system (Fig. 4a) comprises five cooling units, each featuring a 3D-printed NiTi tube within an anti-buckling sleeve (Methods). Operating under ambient conditions, the prototype delivers a 20 °C temperature span and 50 W of cooling power, rivaling systems that use conventionally processed NiTi[13,14,16]. Further demonstrating its robustness, we show in Fig. S20 the prototype's performance both in a one-hour continuous run and over 31500 cumulative cycles (performed over 7 days with 5 h of operation per day).

While our prototype still trails the state-of-the-art system in performance[11], this demonstration verifies the practical applicability of 3D-printed NiTi alloys and establishes a new research paradigm for green elastocaloric systems. By overcoming the fundamental geometric limitations inherent to traditional processing, 3D printing enables a revolutionary transition from constrained planar designs (2D) to 3D-architecture refrigerants (Fig. 4b). This geometric liberation unlocks opportunities for performance optimization through the advanced topological design of internal flow channels, which are critical in determining heat exchange efficiency and performance ceilings.

The aforementioned paradigm shift extends beyond performance considerations, as 3D printing introduces transformative manufacturing advantages (Fig. 4c). Conventional manufacturing employs separated processes: bulk materials undergo multistep thermomechanical treatments for microstructure regulation, followed by sequential subtractive machining of individual structures. In stark contrast, 3D printing allows integrated microstructure–macrostructure co-regulation during fabrication while enabling parallel production of geometrically diverse refrigerants in single batches, thus significantly reducing the production time and costs. Furthermore, its additive nature ensures near-perfect material utilization, overcoming the excessive wastage that characterizes subtractive methods.

These advantages – improved geometric freedom, efficient production, and better material utilization – collectively reshape the development pathway for elastocaloric cooling technologies, establishing a foundation for advanced prototypes that can exploit the capabilities of 3D printing.

Discussion

In summary, we propose, fabricate, and validate high-performance 3D-printed NiTi alloys as elastocaloric refrigerants for sustainable cooling. The proposed alloys exhibit million-cycle durability and high specific temperature change, outperforming commercial NiTi counterparts and existing 3D-printed benchmarks. These advancements are attributed to defect minimization and bimodal microstructures, which concurrently suppress dislocation slip and crack propagation while facilitating reversible phase transformations. Moreover, we successfully integrated 3D-printed NiTi refrigerants into a functional cooling prototype, achieving a temperature span of 20 °C from ambient conditions. These breakthroughs demonstrate the potential of 3D printing's performance-tuning capabilities and manufacturing flexibility to advance the emerging field of solid-state cooling.

Methods

Fabrication of NiTi alloys and tubes

NiTi samples were fabricated via LPBF using an EOS M100 LPBF system with a laser spot diameter of 40 µm. Commercial NiTi powders (nominal composition in at.%: $Ni_{50.8}Ti_{49.2}$, particle size distribution provided in Fig. S21) were deposited onto a NiTi substrate. The optimized LPBF parameters included a laser power (P) of 90 W, a scanning speed (V) of 1000 mm·s^{-1}, a layer thickness (t) of 20 µm, and a hatch spacing (h) of 80 µm, yielding a VED of ~56 J·mm^{-3} ($VED = P/(V{\cdot}t{\cdot}h)$). The build chamber was continuously purged with high-purity argon, which maintained the oxygen content below 0.1% throughout printing. All samples were removed from the substrate via EDM. The subsequent annealing treatment was conducted in an argon-purged tube furnace, where the samples were kept at 950 °C for 1 h before being water-quenched at 22 °C.

Compression testing

Cuboidal samples (2.5 mm × 2.5 mm × 5 mm) were fabricated for compression testing. Cyclic compression tests were conducted at ambient temperature (22 °C) using a servo-hydraulic MTS machine (load capacity of 15 kN). The strain measurements were calibrated via an extensometer to ensure accuracy. To determine the maximum ΔT, a discrete sample was dedicated to each predefined stress level (300–1000 MPa) for a strain rate of 1×10^{-3} s^{-1}, followed by a 20-s stress hold to dissipate the latent heat generated during loading. The temperature evolution during subsequent rapid unloading (duration of 0.2 s, corresponding to strain rates of 0.1–0.2 s^{-1}) was recorded using an FLIR SC7700M infrared camera. Quasi-static compression tests were conducted under identical loading/unloading rates of 5×10^{-4} s^{-1}. For long-term cyclic performance evaluation, the samples were subjected to 3×10^{6} loading cycles at a stress amplitude of 550 MPa and frequency of 20 Hz.

The specific temperature change was calculated as $\Delta T_{spe} = \Delta T/\sigma_{DRI}$. Due to functional degradation, its maximum value typically corresponds to the first-cycle ΔT. To ensure a fair comparison, the maximum ΔT_{spe} values in Fig. 1c are based on the first-cycle ΔT reported for each alloy, except where studies explicitly provided data from a pre-trained sample[38] or a non-first-cycle value[49]. Detailed values can be found in Supplementary Table 1.

Structure characterization

µ-CT was employed to characterize the pore distribution within the cuboidal specimens (2.5 mm × 2.5 mm × 5 mm) using an acceleration voltage of 110 kV and isotropic voxel resolution of 2 µm. For crystallographic analysis, EBSD was performed on 8 mm × 8 mm × 8 mm samples using a field-emission scanning electron microscope (FEI Apreo 2) equipped with an Oxford Instruments EBSD detector. The EBSD samples underwent sequential preparation: mechanical grinding through progressively finer SiC abrasives (up to 5000 grit), followed by electropolishing in a solution of 90% methanol and 10% sulfuric acid. EBSD mapping was conducted at an acceleration voltage of 20 kV with step sizes ranging from 0.05 to 1 µm, optimized according to the magnification requirements. A JEOL JEM-2100F TEM was utilized for further morphological characterization at an acceleration voltage of 200 kV. TEM foils (diameter of 3 mm) were prepared through mechanical thinning to ~50 µm, followed by cryogenic ion milling at −50 °C (GATAN 691). The phase transformation behaviors were determined via differential scanning calorimetry (DSC; Netzsch DSC 200 F3). Samples measuring 2 mm × 2 mm × 1 mm were subjected to a cooling–heating cycle between −80 °C and 80 °C at a constant scanning rate of 10 °C·min^{-1} under a nitrogen purge.

Elastocaloric prototype testing

Figure S22 displays a schematic of the elastocaloric cooling prototype. Each refrigeration unit consists of two 3D-printed components: NiTi tubes and anti-bulking polymer sleeves. The NiTi tubes (diameter of 8.1 mm, length of 50 mm), featuring internal flow channels, were fabricated via LPBF. The polymer sleeves, made from polyethylene terephthalate glycol, were produced through fused filament fabrication using a Bambu Carbon X1 printer. The prototype comprises five units connected in series, with ceramic load-transfer spacers positioned between them. Actuation is provided by a 30-kN PLC-controlled servo actuator under displacement control. Active regenerative cycling at 0.25 Hz was performed to establish the temperature span (ΔT_{span}) between the cold and hot sides. As shown in Fig. S23, this process involves four stages: 1) rapid compression (0.5 s); 2) a holding stage (1.5 s) during which distilled water flowed from the cold-side pump through the tubes to the hot-side reservoir, transferring latent heat; 3) rapid unloading (0.5 s); and 4) another holding stage (1.5 s) during which distilled water flowed from the hot-side pump through the tubes to the cold-side reservoir, transferring latent heat. Temperature was monitored using 80-µm T-type thermocouples immersed in both reservoirs, with data logged using an NI cDAQ-9171 data acquisition system. The cooling power (W) was calculated as $W = \Delta T_{span}{\cdot}\dot{m}{\cdot}C$, where $\dot{m}$ is the mass flow rate, and C is the specific heat capacity of NiTi.

Data availability

Source data are provided with this paper.

References

1. Abas, N. et al. Natural and synthetic refrigerants, global warming: A review. *Renew. Sust. Energ. Rev.* **90**, 557–569 (2018).
2. Qian, S. et al. High-performance multimode elastocaloric cooling system. *Science* **380**, 722–727 (2023).
3. Tušek, J. et al. The elastocaloric effect: a way to cool efficiently. *Adv. Energy Mater.* **5**, 1500361 (2015).
4. Qian, S. et al. A review of elastocaloric cooling: Materials, cycles and system integrations. *Int. J. Refrig.* **64**, 1–19 (2016).
5. Li, L. et al. Cooling innovations: elastocaloric shape memory alloys, manufacturing, simulation, and refrigerator. *Prog. Mater. Sci.* **153**, 101477 (2025).
6. Sharar, D. J., Radice, J., Warzoha, R., Hanrahan, B. & Smith, A. Low-force elastocaloric refrigeration via bending. *Appl. Phys. Lett.* **118**, 184103 (2021).

7. Ianniciello, L., Bartholomé, K., Fitger, A. & Engelbrecht, K. Long life elastocaloric regenerator operating under compression. *Appl. Therm. Eng.* **202**, 117838 (2022).
8. Li, X., Cheng, S. & Sun, Q. A compact NiTi elastocaloric air cooler with low force bending actuation. *Appl. Therm. Eng.* **215**, 118942 (2022).
9. Li, X. et al. High-frequency bending-actuated elastocaloric cooler with enhanced cooling performance. *Cell Rep. Phys. Sci.* **6**, 102669 (2025).
10. Zhou, G., Zhu, Y., Yao, S. & Sun, Q. Giant temperature span and cooling power in elastocaloric regenerator. *Joule* **7**, 2003–2015 (2023).
11. Zhou, G. et al. Achieving kilowatt-scale elastocaloric cooling by a multi-cell architecture. *Nature* **693**, 87–92 (2025).
12. Li, X., Hua, P. & Sun, Q. Continuous and efficient elastocaloric air cooling by coil-bending. *Nat. Commun.* **14**, 7982 (2023).
13. Yao, S. et al. Efficient roller-driven elastocaloric refrigerator. *Nat. Commun.* **15**, 7203 (2024).
14. Tušek, J. et al. A regenerative elastocaloric heat pump. *Nat. Energy* **1**, 1–6 (2016).
15. Zhou, G. et al. A multi-material cascade elastocaloric cooling device for large temperature lift. *Nat. Energy* **9**, 1–9 (2024).
16. Zhang, J. et al. Sustainable all-solid elastocaloric cooler enabled by non-reciprocal heat transfer. *Nat. Sustain.* **8**, 651–660 (2025).
17. Snodgrass, R. & Erickson, D. A multistage elastocaloric refrigerator and heat pump with 28 K temperature span. *Sci. Rep.* **9**, 18532 (2019).
18. Zhou, G. et al. Sub-zero Celsius elastocaloric cooling via low-transition-temperature alloys. *Nature* **649**, 879–884 (2026).
19. Chen, J. et al. Toward tunable mechanical behavior and enhanced elastocaloric effect in NiTi alloy by gradient structure. *Acta Mater.* **226**, 117609 (2022).
20. Zhang, Q. et al. Improved elastocaloric effect of NiTi shape memory alloys strengthened by Ni4Ti3 nanoprecipitates. *Acta Mater.* **281**, 120442 (2024).
21. Dang, P. et al. Low-fatigue and large room-temperature elastocaloric effect in a bulk Ti49.2Ni40.8Cu10 alloy. *Acta Mater.* **229**, 117802 (2022).
22. Lin, H., Hua, P., Huang, K., Li, Q. & Sun, Q. Grain boundary and dislocation strengthening of nanocrystalline NiTi for stable elastocaloric cooling. *Scr. Mater.* **226**, 115227 (2023).
23. Zhong, S. et al. Achieving efficient damping performance tuning in NiTi alloy via laser powder bed fusion. *Acta Mater.* **296**, 121281 (2025).
24. Zhong, S. et al. Superelastic and robust NiTi alloys with hierarchical microstructures by laser powder bed fusion. *Addit. Manuf.* **90**, 104319 (2024).
25. Zhong, S. et al. Superelastic NiTi scaffolds with extensively tunable mechanical and mass transfer properties. *Int. J. Extrem. Manuf.* **7**, 065507 (2025).
26. Zhong, S. et al. Robust and resilient Mg–NiTi interpenetrating-phase composites with triply periodic minimal surface configuration. *J. Magnes. Alloy.* **13**, 4379–4394 (2025).
27. Cao, Y. et al. Large tunable elastocaloric effect in additively manufactured Ni–Ti shape memory alloys. *Acta Mater.* **194**, 178–189 (2020).
28. Zhan, J. et al. Achieving fine tailoring of elastocaloric properties of laser powder bed-fused NiTi alloy via laser beam manipulation. *Int. J. Mach. Tools Manuf.* **202**, 104210 (2024).
29. Chen, C. et al. Elastocaloric effect of NiTi shape memory alloys manufactured by laser powder bed fusion. *J. Mater. Res. Technol.* **33**, 3439–3451 (2024).
30. Hou, H. et al. Elastocaloric cooling of additive manufactured shape memory alloys with large latent heat. *J. Phys. D: Appl. Phys.* **50**, 404001 (2017).
31. Wan, X., Feng, Y., Lin, X. & Tan, H. Large superelastic recovery and elastocaloric effect in as-deposited additive manufactured Ni50.8Ti49.2 alloy. *Appl. Phys. Lett.* **114**, 221903 (2019).
32. Kordizadeh, F. et al. Investigating the elastocaloric effect of the NiTi fabricated by laser powder bed fusion: Effect of the building orientation. *Materialia* **30**, 101817 (2023).
33. Zhan, J. et al. Unleashing the elastocaloric cooling potential of 3D-printed NiTi alloy with heterogeneous microstructures and Ni4Ti3 nanoparticles. *Compos. Pt. B-Eng.* **288**, 111918 (2024).
34. Zhang, M., Fang, X., Li, X., Li, Z. & Huang, K. Tailorable elastocaloric cooling performance of wire-arc directed energy deposition NiTi alloy through concentration gradient design. *J. Mater. Sci. Technol.* **226**, 229–244 (2025).
35. Wang, S. et al. Microstructure and elastocaloric effect of NiTi shape memory alloy in-situ synthesized by laser directed energy deposition additive manufacturing. *Mater. Charact.* **210**, 113831 (2024).
36. Wang, S. et al. Tailoring microstructure and strengthening mechanism of anisotropic elastocaloric effect in NiTi shape memory alloys by laser directed energy deposition scanning strategy. *J. Mater. Process. Technol.* **339**, 118825 (2025).
37. Li, K. et al. Elastocaloric effect of laser powder bed fused NiTi alloy with customizable hierarchical heterogeneous microstructure. *Addit. Manuf.* **97**, 104619 (2025).
38. Hou, H. et al. Fatigue-resistant high-performance elastocaloric materials made by additive manufacturing. *Science* **366**, 1116–1121 (2019).
39. Lin, H., Hua, P. & Sun, Q. Effects of grain size and partial amorphization on elastocaloric cooling performance of nanostructured NiTi. *Scr. Mater.* **209**, 114371 (2022).
40. Chen, J., Xing, L., Fang, G., Lei, L. & Liu, W. Improved elastocaloric cooling performance in gradient-structured NiTi alloy processed by localized laser surface annealing. *Acta Mater.* **208**, 116741 (2021).
41. Hua, P., Chu, K., Ren, F. & Sun, Q. Cyclic phase transformation behavior of nanocrystalline NiTi at microscale. *Acta Mater.* **185**, 507–517 (2020).
42. Dan, C. et al. Achieving ultrahigh fatigue resistance in AlSi10Mg alloy by additive manufacturing. *Nat. Mater.* **22**, 1182–1188 (2023).
43. Qu, Z. et al. High fatigue resistance in a titanium alloy via near-void-free 3D printing. *Nature* **626**, 999–1004 (2024).
44. Liu, H. et al. Review on Fatigue of Additive Manufactured Metallic Alloys: Microstructure, Performance, Enhancement and Assessment Methods. *Adv. Mater.* **36**, e2306570 (2024).
45. DebRoy, T. et al. Additive manufacturing of metallic components – Process, structure and properties. *Prog. Mater. Sci.* **92**, 112–224 (2018).
46. Chu, K. & Sun, Q. Reducing functional fatigue, transition stress and hysteresis of NiTi micropillars by one-step overstressed plastic deformation. *Scr. Mater.* **201**, 113958 (2021).
47. Wei, S. et al. Laser powder bed fusion additive manufacturing of NiTi shape memory alloys: A review. *Int. J. Extrem. Manuf.* **25**, 032001 (2023).
48. Pu, Z. et al. Study on the role of carbon in modifying second phase and improving tensile properties of NiTi shape memory alloys fabricated by electron beam directed energy deposition. *Addit. Manuf.* **75**, 103733 (2023).
49. Zhang, K., Kang, G. & Sun, Q. High fatigue life and cooling efficiency of NiTi shape memory alloy under cyclic compression. *Scr. Mater.* **159**, 62–67 (2019).
50. Zhu, Y. et al. Heterostructured materials: superior properties from hetero-zone interaction. *Mater. Res. Lett.* **9**, 1–31 (2020).
51. Ma, E. & Zhu, T. Towards strength–ductility synergy through the design of heterogeneous nanostructures in metals. *Mater. Today* **20**, 323–331 (2017).

52. Chen, J., Yin, H. & Sun, Q. Effects of grain size on fatigue crack growth behaviors of nanocrystalline superelastic NiTi shape memory alloys. *Acta Mater.* **195**, 141–150 (2020).
53. Xie, G. et al. Grain size dependence of cracking performance in polycrystalline NiTi alloys. *J. Alloy. Compd.* **884**, 161132 (2021).
54. Baxevanis, T., Parrinello, A. F. & Lagoudas, D. C. On the fracture toughness enhancement due to stress-induced phase transformation in shape memory alloys. *Int. J. Plast.* **50**, 158–169 (2013).
55. Ahadi, A. & Sun, Q. Grain size dependence of fracture toughness and crack-growth resistance of superelastic NiTi. *Scr. Mater.* **113**, 171–175 (2016).
56. Yang, C. et al. Large recoverable strains with high recovery rates via cooperative regulation of texture and precipitation in additive manufactured NiTi alloy. *Scr. Mater.* **248**, 116122 (2024).
57. Otsuka, K. & Ren, X. Physical metallurgy of Ti–Ni-based shape memory alloys. *Prog. Mater. Sci.* **50**, 511–678 (2005).
58. Pu, Z. et al. In-situ synthesis of NiTi shape memory alloys with tunable chemical composition and thermomechanical response by dual-wire-feed electron beam directed energy deposition. *J. Mater. Sci. Technol.* **216**, 209–225 (2025).
59. Tomozawa, M., Kim, H. Y. & Miyazaki, S. Shape memory behavior and internal structure of Ti–Ni–Cu shape memory alloy thin films and their application for microactuators. *Acta Mater.* **57**, 441–452 (2009).
60. Wang, Z. et al. Grain Structure Engineering of NiTi Shape Memory Alloys by Intensive Plastic Deformation. *ACS Appl. Mater. Interfaces* **14**, 31396–31410 (2022).

Acknowledgements

This work was supported by National Key Research and Development Program of China (2024YFA1208004 (J. Lu)), Hong Kong JLFS - RGC-Joint Laboratory Funding Scheme (Grant No. JLFS/E-102/24 (J. Lu)), Guangdong Province Science and Technology Plan Project 2023B1212120008 (J. Lu), Hong Kong RGC Strategic Topic Grant (Grant No. STG2-E-605-23-N (Q. Sun)), and Hong Kong Research Grant Council (GRF projects No. 16204422 (S. Yao)). J. Lu thanks for the IMR-CityU Joint Laboratory of Nanomaterials & Nanomechanics and Guangdong-Hong Kong Joint Laboratory of Modern Surface Engineering Technology.

Author contributions

S.Z.: Conceptualization, Investigation, Writing – original draft, Visualization. H.L.: Methodology, Investigation, Writing – original draft, Visualization. Y.L.: Methodology, Investigation, Visualization. Y.L.: Writing – review & editing, Visualization. G.Z.: Formal analysis, Methodology. P.Z.: Investigation. L.Z.: Writing – review & editing. S.W.: Writing – review & editing. S.Y.: Funding acquisition, Resources, Supervision, Writing – review & editing. Q.S.: Funding acquisition, Resources, Supervision, Writing – review & editing. J.L.: Conceptualization, Funding acquisition, Project administration, Resources, Supervision, Writing – review & editing.

Competing interests

The authors declare no competing interests.

Additional information

Supplementary information The online version contains supplementary material available at https://doi.org/10.1038/s41467-026-71399-8.

Correspondence and requests for materials should be addressed to Shuhuai Yao, Qingping Sun or Jian Lu.

Peer review information *Nature Communications* thanks Emre Acar, Kadri Atli and the other, anonymous, reviewer(s) for their contribution to the peer review of this work. A peer review file is available.